

This is the accepted manuscript made available via CHORUS. The article has been published as:

# Giant Narrow-Band Optical Absorption and Distinctive Excitonic Structures of Monolayer

$$\frac{C}{N^3}$$
 and 
$$\frac{C}{B^3}$$

Zhao Tang, Greis J. Cruz, Yabei Wu, Weiyi Xia, Fanhao Jia, Wenqing Zhang, and Peihong Zhang

Phys. Rev. Applied **17**, 034068 — Published 28 March 2022

DOI: [10.1103/PhysRevApplied.17.034068](https://doi.org/10.1103/PhysRevApplied.17.034068)

# Giant narrow-band optical absorption and distinctive excitonic structures of monolayer C<sub>3</sub>N and C<sub>3</sub>B

Zhao Tang,<sup>1</sup> Greis J. Cruz,<sup>1</sup> Yabei Wu,<sup>2</sup> Weiyi Xia,<sup>3</sup> Fanhao Jia,<sup>1,4</sup> Wenqing Zhang,<sup>2</sup> and Peihong Zhang<sup>1\*</sup>

<sup>1</sup>*Department of Physics, University at Buffalo, State University of New York, Buffalo, New York 14260, USA*

<sup>2</sup>*Department of Materials Science and Engineering, Shenzhen Institute for Quantum Science and Engineering, and Academy for Advanced Interdisciplinary Studies, Southern University of Science and Technology, Shenzhen, Guangdong 518055, China*

<sup>3</sup>*Department of Physics and Astronomy, Iowa State University, Ames, Iowa 50011, USA*

<sup>4</sup>*School of Materials Science and Engineering & International Centre of Quantum and Molecular Structures, Shanghai University, Shanghai 200444, China*

\*E-mail: [pzhang3@buffalo.edu](mailto:pzhang3@buffalo.edu)

## Abstract

Low dimensional materials provide a unique platform for exploring exotic properties that are otherwise unachievable in bulk solids. C<sub>3</sub>N and C<sub>3</sub>B are two graphene-derived two-dimensional (2D) ordered alloys that have attracted increasing research attention. These materials are best known for their remarkable stability and moderate band gaps, and thus are suitable for a range of applications. Perhaps the most interesting feature of the electronic structures of C<sub>3</sub>N and C<sub>3</sub>B is the existence of nearly parallel valence and conduction bands across a large region of the Brillouin zone. In this work, using many-body perturbation theory within the GW and Bethe-Salpeter equation (BSE) approach, we predict that the primarily  $p_z$  orbitals derived nearly parallel valence and conduction bands in monolayer C<sub>3</sub>N and C<sub>3</sub>B give rise to a giant narrow-band absorption peak in their optical absorption spectra. More surprisingly, two degenerate excitonic states contribute to over 90% and 80% of the dipole absorption below 5 eV for C<sub>3</sub>N and C<sub>3</sub>B, respectively. Detailed examinations of the exciton binding energies unveil a unique shell-like distribution of the excitonic states, with each shell (series) converging to a different excitation edge. Such distinctive absorption properties have not been observed in any other 2D materials. We further investigate the internal structure of the excitonic states using a multifaceted approach and reveal several important characteristics of the excitonic states in these 2D materials.

## 1. Introduction

The research on graphene [1] has opened the era of two-dimensional (2D) materials [2-8] with extraordinary properties beyond what are offered by traditional bulk (3D) materials. The defining electronic structure of graphene, however, also limits its applications in electronic devices, and much recent effort has been devoted to the search for graphene-like (or graphene-based) 2D semiconductors. One possibility is to incorporate compatible heteroatoms such as boron and/or nitrogen into graphene. [9-13] Since both B and N form  $sp^2$  bonds, the introduction of these atoms does not significantly affect the hexagonal network of graphene, but, at the same time, offers the possibility of opening up a sizable band gap for electronic or energy applications.

In fact, a number of ordered graphitic borocarbonitride alloys have been proposed and/or synthesized; examples include  $C_2N$ , [14]  $C_3N$ , [15-18]  $C_3B$ , [19-22]  $C_5N$ , [23]  $C_4N_3$ , [24] graphitic  $C_3N_4$ , [25,26] and  $BC_6N$ . [27-30] Among them,  $C_3N$  and  $C_3B$  are two particularly interesting ones due to their remarkable stability, moderate band gaps, and high alloy contents while maintaining a nearly ideal hexagonal network. Low dimensional materials such as  $C_3N$  and  $C_3B$  can also serve as an interesting platform for studying the exciton physics. Perhaps one of the most interesting features of the electronic structures of  $C_3N$  and  $C_3B$  is the existence of nearly parallel valence and conduction bands across a large region of the Brillouin zone (BZ). [15,18,21,22] Unlike direct gap 2D semiconductors such as black phosphorus and  $MoS_2$ , in which the low energy excitonic states are derived from (non-interacting) electron-hole ( $e-h$ ) pairs that are highly concentrated in a small region(s) of the BZ around the direct-gap  $k$ -point(s), [31,32] the  $k$ -space spread of the low energy exciton wave functions in  $C_3N$  and  $C_3B$  can be far more extended, offering the possibility of strong and narrow-band optical absorption.

In this work, we investigate the optical properties and excitonic structures of monolayer  $C_3N$  and  $C_3B$ . The quasiparticle band structures are calculated using the GW [33] approximation; the  $e-h$  excitations and optical properties are obtained by solving the Bethe-Salpeter equation (BSE). [34] We find that two low-energy degenerate excitonic states contribute to over 90% and 80% of the dipole absorption below 5 eV for  $C_3N$  and  $C_3B$ , respectively. To the best of our knowledge, no other known materials have such intriguing optical properties. We also examine the state-specific exciton binding energies of  $C_3N$  and  $C_3B$  for all excitonic states below 5 eV and uncover an interesting pattern for the distribution of excitonic states: pairs of nearly parallel valence and conduction bands give rise to a shell-like distribution of exciton states with similar non-interacting  $e-h$  excitation energies (defined later) but with disparate exciton binding energies. Excitonic states with large binding energies (1 eV or larger) are observed within each shell (series), suggesting that strongly bound excitonic states can form well above the fundamental band gap. We further investigate the formation mechanism of the excitonic states in  $C_3N$  and  $C_3B$  by analyzing their band, energy and reciprocal space and unveil several important characteristics of the excitonic wave functions in these systems. These results will help shed light on the formation mechanism of excitonic states in indirect band gap 2D semiconductors.

## 2. Computational details

The quasiparticle band structures are calculated within the GW [33] approximation, and the  $e$ - $h$  excitations and optical properties are obtained by solving the BSE [34], using a local version of the BerkeleyGW code [34,35]. These many-body perturbation calculations are carried out starting from the density functional theory (DFT) mean-field solution within the local density approximation (LDA) [36-38]. Our work benefits from the recently developed acceleration methods [39,40] that lead to a combined speed-up factor of over three orders of magnitude for GW calculations of 2D materials.

We include a large vacuum layer of 40 a.u. and use a truncated Coulomb potential [41] in our calculations to minimize the fictitious interaction between periodic image layers. The Hybertsen-Louie Generalized Plasmon-Pole (HL-GPP) model [33] is used to extend the static dielectric function to finite frequencies. A cutoff energy of 60 Ry is used for the DFT pseudopotential plane wave calculations, and we use a high kinetic cutoff of 40 Ry for the dielectric matrices. Excitonic structure calculations often require an extremely dense  $k$ -grid to properly converge the result. With a good balance of accuracy and efficiency, we applied a dual-grid method [34] to reduce the workload: The electron  $e$ - $h$  kernel is first calculated on an  $18 \times 18 \times 1$  coarse  $k$ -grid, the results are then interpolated onto a  $60 \times 60 \times 1$  fine  $k$ -grid. The density of the fine grid for the 8-atom unit-cell  $C_3N$  and  $C_3B$  is equivalent to that of a  $120 \times 120 \times 1$   $k$ -grid for a 2-atom graphene unit cell. We only investigate excitons with zero wave vectors (i.e., vertical transitions) in this work. For the optical absorption calculations, we assume an in-plane polarization. The optical properties of these two materials are 2D isotropic. Other details of the calculations will be discussed later.

## 3. Results and discussion

### 3.1 Quasiparticle and optical properties: Nearly parallel quasiparticle band structures and giant narrow-band optical absorption

We use the van der Waals functional optB86b-vdW [42] to optimize the crystal structures [shown schematically in Figure 1(a)]; the optimized lattice constants for  $C_3N$  and  $C_3B$  are 4.857 Å and 5.170 Å, respectively. These structures are used for subsequent GW plus BSE calculations. Figure 1(b) compares the DFT-LDA and GW quasiparticle band structures of  $C_3N$  and  $C_3B$ . Our GW calculations take advantage of the recent developments [39,40] that drastically reduce the computation efforts for 2D materials. Using the energy-integration technique, [39] we are able to include *all* conduction bands in the GW calculations at a fraction of the computational effort compared with the conventional band-by-band summation approach. The combined mini-Brillouin zone subsampling and analytical integration technique, [40] on the other hand, greatly improves the BZ sampling efficiency for GW calculations of 2D materials. Details of the convergence tests can be found in our previous publications [18,22]. Our converged GW calculations give a minimum (indirect) band gap of 1.51 eV for  $C_3N$  and 2.44 eV for  $C_3B$ , and the direct minimum band gaps ( $E_g^{\text{dir}}$ ) are 2.68 eV and 2.98 eV for  $C_3N$  (between  $\Gamma$  and M) and  $C_3B$  (at M), respectively.

One of the most distinctive features of the quasiparticle band structures of  $C_3N$  and  $C_3B$  [Figure 1 (b)] is the presence of nearly parallel low energy valence and conduction bands as shown in Figure 1 (b). To better illustrate this point, we show in Figure 1 (c) the contour color maps of the direct quasiparticle gaps between the top valence and bottom conduction bands. The black curves highlight the area in the BZ in which the non-interacting  $e$ - $h$  pair excitation energy is within 0.2 eV from the minimum direct gap  $E_g^{\text{dir}}$ . Compared with the direct band gap semiconductors which often have low joint density of states (JDOS) at the adsorption edge, the JDOS of indirect band gap materials with parallel band edges can be significantly higher. Consequently, a large number of  $e$ - $h$  pairs with similar (non-interacting) excitation energies are available. If the transitions between these bands are optical allowed, we expect the formation of excitonic states with much stronger optical absorption compared with direct band gap 2D semiconductors.

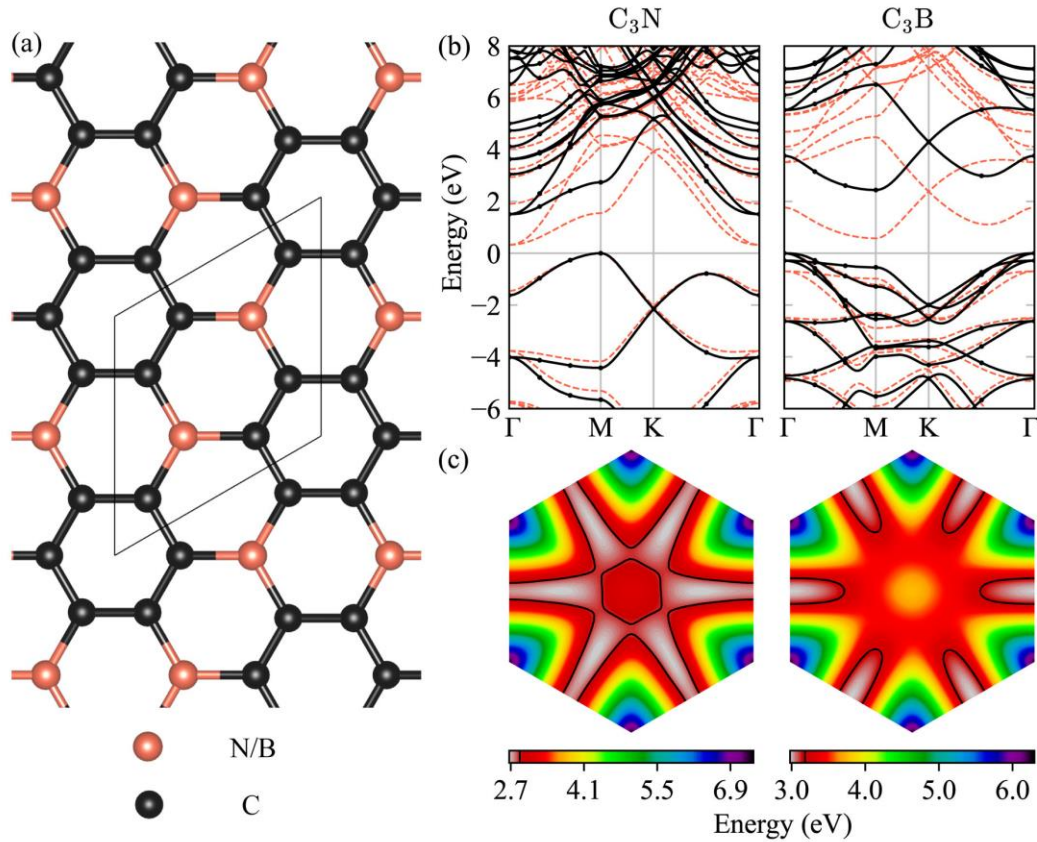


Figure 1. Crystal structures and band structures of  $C_3N$  and  $C_3B$ . (a) Crystal structures of  $C_3N$  and  $C_3B$ . Note that small distortions from the ideal graphene structure are not shown for simplicity. (b) DFT (orange dashed lines) and GW (black solid lines) band structures. The valence band maximum (VBM) has been shifted to zero. (c) Contour color maps (in the Brillouin zone) of the direct quasiparticle band gap between the top valence and bottom conduction bands; the minimum direct band gap ( $E_g^{\text{dir}}$ ) is shown with light gray. The nearly parallel valence and conduction bands give rise to extended areas (light gray areas highlighted with black contour curves) in which the quasiparticle excitation energies are within 0.2 eV to  $E_g^{\text{dir}}$ .

We then investigate the  $e$ - $h$  excitations and optical properties of C<sub>3</sub>N and C<sub>3</sub>B by solving the BSE equation, which is reduced to an eigenvalue problem after decoupling the excitations and de-excitations: [34]

$$(E_{ck} - E_{vk})A_{vck}^S + \sum_{v'c'k'} \langle vck | K^{eh} | v'c'k' \rangle A_{v'c'k'}^S = \Omega^S A_{vck}^S, \quad (1)$$

where  $E_{ck}$  and  $E_{vk}$  are the quasiparticle energies of the conduction and valence states calculated within the GW approximation, and  $K^{eh}$  is the electron-hole interaction kernel. Solving the above eigenvalue problem gives the  $e$ - $h$  excitation energies  $\Omega^S$  and the corresponding eigenvectors  $A_{vck}^S$ , from which the excitonic wave functions can be constructed:

$$\psi^S(\mathbf{r}_e, \mathbf{r}_h) = \sum_{vck} A_{vck}^S \psi_{ck}(\mathbf{r}_e) \psi_{vk}^*(\mathbf{r}_h). \quad (2)$$

The imaginary part of the macroscopic transverse dielectric function, which describes the interaction between the  $e$ - $h$  excitations and an external light field, is given by

$$\epsilon_2(\omega) = \frac{16\pi^2 e^2}{\omega^2} \sum_S |\vec{e} \cdot \langle 0 | \vec{v} | S \rangle|^2 \delta(\omega - \Omega^S), \quad (3)$$

where  $\vec{v}$  is the velocity operator and  $\vec{e}$  is the polarization vector of the light. In practical calculations, we use a Gaussian function with a broadening parameter of 0.05 eV in place of the delta function.

Our GW plus BSE calculations indeed show that these valence and conduction states (free  $e$ - $h$  pairs) with close excitation energies can couple coherently to produce exceptionally strong optical absorption, as shown in Figure 2 (b). The full excitonic spectrum is shown in Figure 2 (a) as vertical lines color coded with the magnitude of the dipole matrix elements (squared) of the excitonic states. The calculated imaginary part of the dielectric functions of C<sub>3</sub>N (left panel) and C<sub>3</sub>B (right panel) are highly unusual in several ways. First, other than the first giant absorption peak (peak A), optical absorption is practically negligible below 5 eV. This is very different from the optical absorption of other materials (2D or bulk), where one often observes, in addition to the below-edge absorptions of bound excitonic states, a gradual increase in the absorption weight above the band edge. Second, the A absorption peak comes almost exclusively from two degenerate exciton states. In Figure 2 (b), we show the state-dependent dipole matrix element (renormalized to one unit-cell), with degenerate states indicated by red circles and non-degenerate states by black circles. A pair of degenerate excitonic states contribute to over 90% and 80% of all dipole absorption weight below 5 eV in C<sub>3</sub>N and C<sub>3</sub>B, respectively. To the best of our knowledge, no other materials show such peculiar optical absorption properties.

The surprisingly weak optical absorption (except for the abnormally strong and nearly monochromatic excitonic absorption peak A) below 5 eV is not a result of the lack of available  $e$ - $h$  pairs in this energy window. In fact, there is a large number of excitonic states with energies below

$E_g^{\text{dir}}$  as shown in Figure 2 (a) and Figure 2 (b). However, most of these states have very small dipole transition matrix elements, hence they can practically be ascribed as dark excitons. Figure 2 (c) shows both the quasiparticle JDOS (i.e., non-interacting  $e$ - $h$  pair density of states) and the exciton density of states (DOS) of  $\text{C}_3\text{N}$  and  $\text{C}_3\text{B}$ . It is clear that there are significant state densities below 5 eV. Except for the formation of a few bound states below the band gap (which only show up as tails due to the broadening technique used in the calculation of the DOS), the main difference between the quasiparticle JDOS and excitonic DOS is a systematic shift in the energy of about 0.2 eV. This shift should reveal the averaged  $e$ - $h$  interaction strength in this energy window. Therefore, it is the coherent (constructive) superpositions of the dipole matrix elements in these 2D materials with nearly parallel band structures that somehow lumps most of the optical absorption weight into one pair of degenerate excitonic states. In the next section, we investigate the details of the excitonic structures and binding energies of  $\text{C}_3\text{N}$  and  $\text{C}_3\text{B}$ .

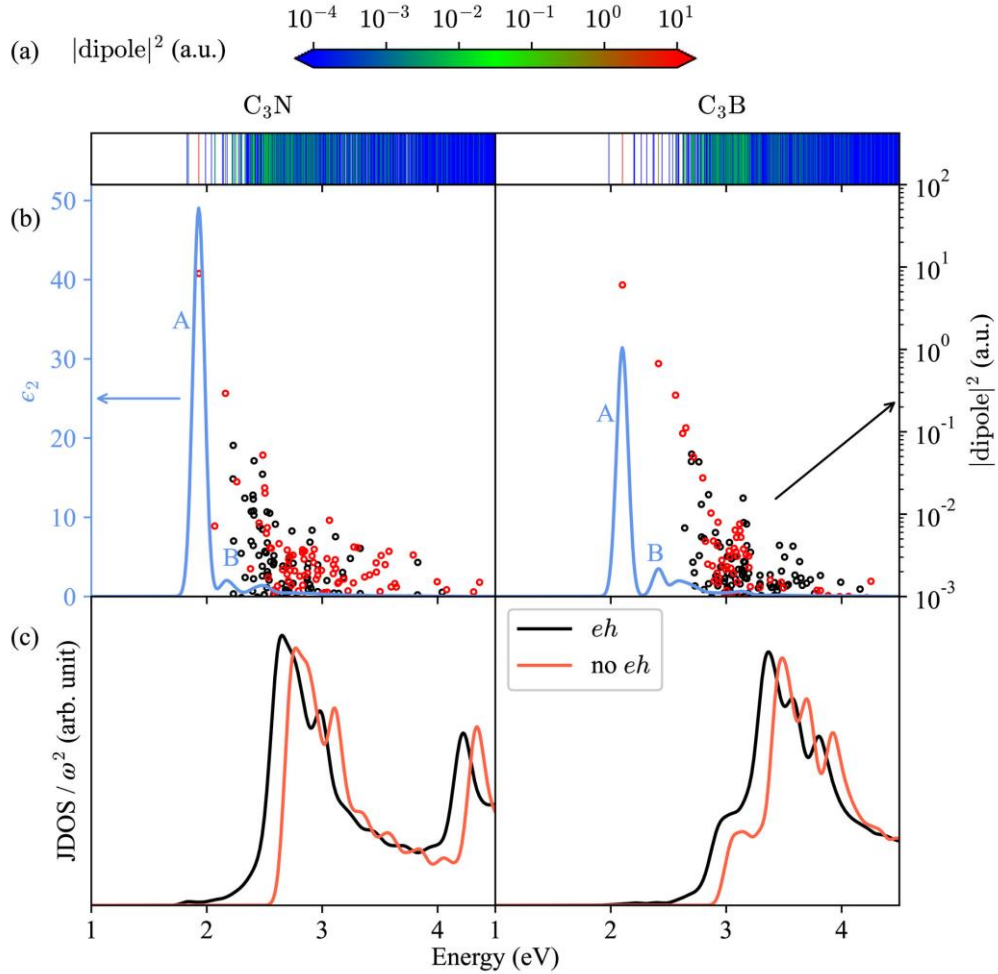


Figure 2. Optical properties of  $\text{C}_3\text{N}$  and  $\text{C}_3\text{B}$ . (a) Distribution of excitonic states within a 5 eV energy window, color coded using the dipole matrix elements. (b) Imaginary part of the dielectric function (solid light blue curve) and dipole matrix elements (red/black circles) of the (degenerated/non-degenerated) excitonic states. (c) Quasiparticle (orange) and excitonic (black) joint density of states (JDOS).

### 3.2 Excitonic structures and shell-like distribution of the exciton binding energies

In addition to the optical absorption discussed in the previous section, it is also of great interest to understand the binding energies of the excitonic states. For direct band gap semiconductors, the textbook definition of the exciton binding energy of a bound excitonic state  $|S\rangle$  below the band gap is the difference between the excitation energy  $\Omega^S$  and the minimum (direct) quasiparticle gap  $E_g^{\text{dir}}$  (i.e., the onset of the excitonic continuum):  $E_b^S = E_g^{\text{dir}} - \Omega^S$ . This definition is also the basis of experimental measurements of the binding energies of the bound states. [Note that here the term bound state is used to distinguish discrete excitonic states below the fundamental gap from the excitonic continuum, which shall not be confused with bound excitons which are referred to excitons bound to certain defects.] One fundamental issue of this simplified definition is that the excitonic wave functions are superpositions of a large number of free (i.e., non-interacting)  $e$ - $h$  pairs, not just the  $e$ - $h$  pair across the minimum gap, as shown in Eq. (2). Thus this definition does not give an accurate understanding of the strength of the  $e$ - $h$  interaction. In addition, this definition does not provide a convenient means to estimate the binding energies of continuum states or bound states that are embedded in (or in resonance with) the continuum.

A more rigorous definition for the exciton binding energy is

$$E_b^S = E_g^S - \Omega^S, \quad (4)$$

where  $E_g^S$  is the expectation value of the free  $e$ - $h$  excitation gap for a given excitonic state  $|S\rangle$ , which can be easily evaluated using the  $e$ - $h$  pair amplitude  $A_{vck}^S$  defined in Eq. (1):

$$E_g^S = \sum_{vck} |A_{vck}^S|^2 (E_{ck} - E_{vk}). \quad (5)$$

The interpretation for Eq. (4) is clear: the exciton binding energy is the difference between the non-interacting and interacting  $e$ - $h$  excitation energies. This definition can be applied to calculating the binding energy of any excitonic states, including bound states below the quasiparticle excitation gap, continuum states, and bound states in resonance with (embedded in) the continuum.

Figure 3 (a) shows the calculated exciton binding energies for  $\text{C}_3\text{N}$  (left) and  $\text{C}_3\text{B}$  (right) vs  $E_g^S$  defined in Eqs. (4) and (5). There are several interesting features that deserve careful examination. First, both systems show distinctive shell-like structures. For  $\text{C}_3\text{N}$ , we can identify five excitonic series (we only label the first three for clarity) below 6 eV. These series stand out as groups of excitonic states with similar  $E_g^S$  but significantly varied exciton binding energies, with each series converging to a different excitation edge. The same series (grouping) behavior can also be seen when we plot the exciton binding energy with respect to the excitation energy  $\Omega^S$ , as shown in Figure 3 (b). For  $\text{C}_3\text{B}$ , at least two series, labeled I, and II, can be clearly recognized. Within each series, excitonic states with large binding energies (around 1 eV or greater) can be observed. This suggests that strongly bound (or resonance) states can form well above the fundamental gap. These



shell-like structures can be traced back to the presence of nearly-parallel valence and conduction bands in these systems. To illustrate this point, we show in Figure 4 the quasiparticle band structures of  $C_3N$  and  $C_3B$  with transitions that are responsible for the excitonic series, indicated by vertical arrows. However, this simplified picture does not show the full detail and complexity of the excitonic states, as discussed in the next section.

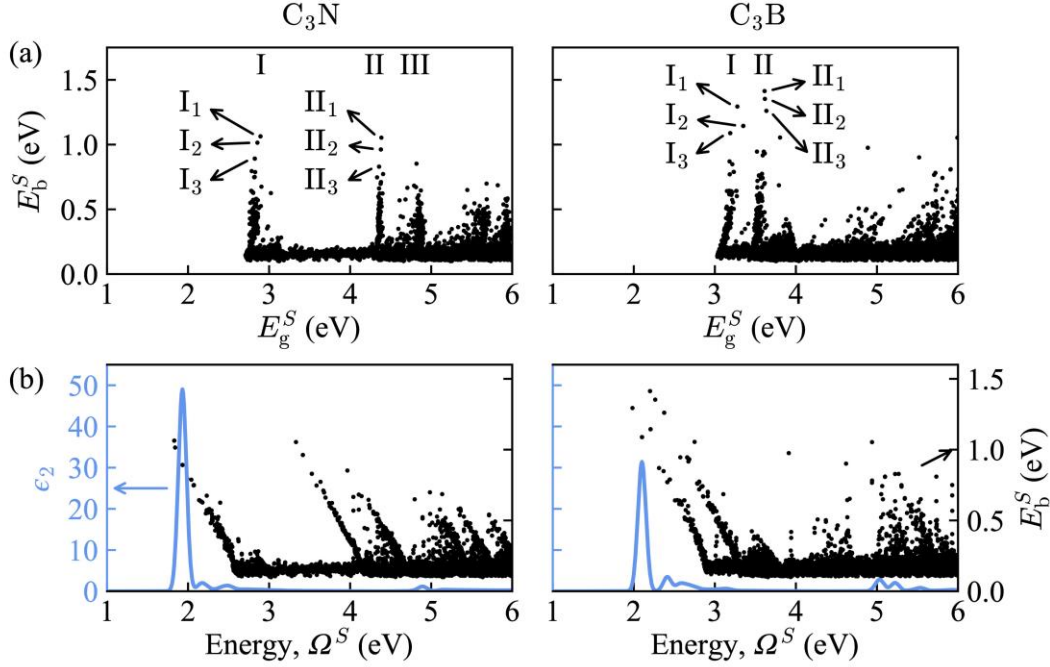


Figure 3. Shell-like distribution of excitonic states in  $C_3N$  and  $C_3B$ . (a) Exciton binding energy with respect to the non-interacting excitation energy  $E_g^S$ . (b) Exciton binding energy with respect to  $\Omega^S$ . The binding energy reveals interesting shell-like distributions, labeled series I, II, and III. In panel (b), we also show the imaginary part of the dielectric function (solid blue curves) to corroborate the positions of the excitonic states.

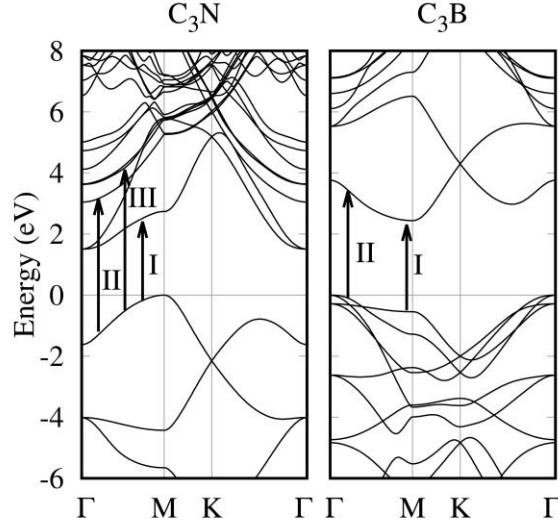


Figure 4. Quasiparticle band structures of  $C_3N$  and  $C_3B$  showing transitions that are responsible for the excitonic series shown in Figure 3.

Another interesting observation from the results shown in Figure 3 is that there are only a small number of excitonic states that have large exciton binding energy: for excitation energies  $\Omega^S < 6$  eV, there are only about 50 states that have exciton binding energies greater than 0.6 eV. In fact, a majority of the excitonic states have binding energies smaller than 0.3 eV. Finally, in addition to the bound states below the energy gap (which are well-understood), each series has its own excitonic bound (or resonance) states and continuum. These large-binding-energy excitonic states above the band gap can be considered as resonance states embedded in the excitonic continuum. Some of these states can have very large binding energies that are comparable to (or even greater than) those below-edge bound states, as shown in Figure 3. Table 1 lists the calculated exciton eigenvalues  $\Omega^S$ , non-interacting excitation energies  $E_g^S$ , binding energies  $E_b^S$ , and the dipole matrix element squared for five states each from series I and II with the largest binding energies for both  $C_3N$  and  $C_3B$ . Even though the energies of the II series excitons are well above the band gaps, states with very large binding energies are observed in this series, suggesting that strongly bound excitons can form well above the quasiparticle band gap. The degenerate  $I_3$  states (responsible for giant optical absorption discussed in the previous section) stand out as the sole state with a very large optical dipole matrix element for both systems.

Table 1. Large-binding-energy excitons from series I and II of C<sub>3</sub>N and C<sub>3</sub>B. For each excitonic state, in addition to the exciton binding energy  $E_b^S$ , we also include the excitation energy  $\Omega^S$ , the non-interacting  $e$ - $h$  excitation energy  $E_g^S$ , the dipole matrix element squared (in a.u.), and the degree of degeneracy. All energies are in electron-Volts (eV).

C <sub>3</sub> N						C <sub>3</sub> B					
	$\Omega^S$	$E_g^S$	$E_b^S$	dipole  <sup>2</sup>	Deg.		$\Omega^S$	$E_g^S$	$E_b^S$	dipole  <sup>2</sup>	Deg.
I <sub>1</sub>	1.830	2.894	1.064	2.18×10 <sup>-6</sup>	2	I <sub>1</sub>	1.984	3.278	1.294	9.31×10 <sup>-5</sup>	1
I <sub>2</sub>	1.841	2.856	1.015	6.57×10 <sup>-4</sup>	1	I <sub>2</sub>	2.206	3.350	1.144	8.80×10 <sup>-8</sup>	2
I <sub>3</sub> (A)	1.932	2.823	0.892	8.35×10 <sup>0</sup>	2	I <sub>3</sub> (A)	2.101	3.190	1.088	6.06×10 <sup>0</sup>	2
I <sub>4</sub>	1.990	2.785	0.795	5.55×10 <sup>-5</sup>	1	I <sub>4</sub>	2.311	3.182	0.870	1.00×10 <sup>-6</sup>	1
I <sub>5</sub>	2.041	2.828	0.788	1.04×10 <sup>-4</sup>	1	I <sub>5</sub>	2.367	3.215	0.848	7.01×10 <sup>-5</sup>	1
II <sub>1</sub>	3.332	4.385	1.054	4.23×10 <sup>-15</sup>	1	II <sub>1</sub>	2.200	3.614	1.413	4.56×10 <sup>-15</sup>	2
II <sub>2</sub>	3.417	4.379	0.962	1.17×10 <sup>-14</sup>	2	II <sub>2</sub>	2.264	3.618	1.353	6.69×10 <sup>-15</sup>	1
II <sub>3</sub>	3.527	4.357	0.830	1.63×10 <sup>-17</sup>	2	II <sub>3</sub>	2.375	3.636	1.261	1.61×10 <sup>-16</sup>	2
II <sub>4</sub>	3.634	4.407	0.772	7.29×10 <sup>-17</sup>	1	II <sub>4</sub>	2.574	3.519	0.946	2.10×10 <sup>-17</sup>	1
II <sub>5</sub>	3.586	4.332	0.747	1.45×10 <sup>-20</sup>	1	II <sub>5</sub>	2.659	3.604	0.945	9.41×10 <sup>-16</sup>	2

### 3.3 Formation of excitonic states: spreads in bands, mode excitations in reciprocal space, and energy distributions

The complexity of the exciton wave functions [Eq. (2)] often makes it difficult to examine the internal structures of the excitonic states. One can inspect the wave functions in real space (by fixing either the electron or the hole position) and gain some visual understanding of the spread and spatial distribution of the electron or hole charge density. However, often we are interested in understanding how the excitonic states are formed from the free  $e$ - $h$  pairs, i.e., the valence and conduction states that compose a given excitonic state. To this end, we propose that the electron and hole amplitude functions defined below would better serve the purpose. For a given excitonic states  $|S\rangle$ , we define three amplitude functions: the band and  $k$ -dependent electron amplitude,

$$|A_{ck}^S|^2 = \sum_v |A_{vck}^S|^2, \quad (6)$$

the hole amplitude,

$$|A_{vk}^S|^2 = \sum_c |A_{vck}^S|^2, \quad (7)$$

and the  $k$ -dependent pair amplitude,

$$|A^S(\mathbf{k})|^2 = \sum_{vc} |A_{vck}^S|^2. \quad (8)$$

The left three panels of Figure 5 show the distributions of  $|A_{ck}^S|^2$  (in blue) and  $|A_{vk}^S|^2$  (orange) for a few excitonic states [labeled I<sub>1</sub>, I<sub>3</sub>, and II<sub>1</sub>, as indicated in Figure 3 (a)] with large binding energies

(i.e., low excitation energies) for C<sub>3</sub>N (top panels) and C<sub>3</sub>B (bottom panels). These plots clearly reveal the band origins of the excitonic states. For example, the I series excitonic states of C<sub>3</sub>N are primarily derived from the nearly-parallel highest valence and lowest conduction bands around the  $\Gamma$ -M and  $\Gamma$ -K paths; the II series, on the other hand, are predominantly derived from the top valence and the third conduction bands. Contributions from other bands and from different regions of the BZ are less significant but still noticeable.

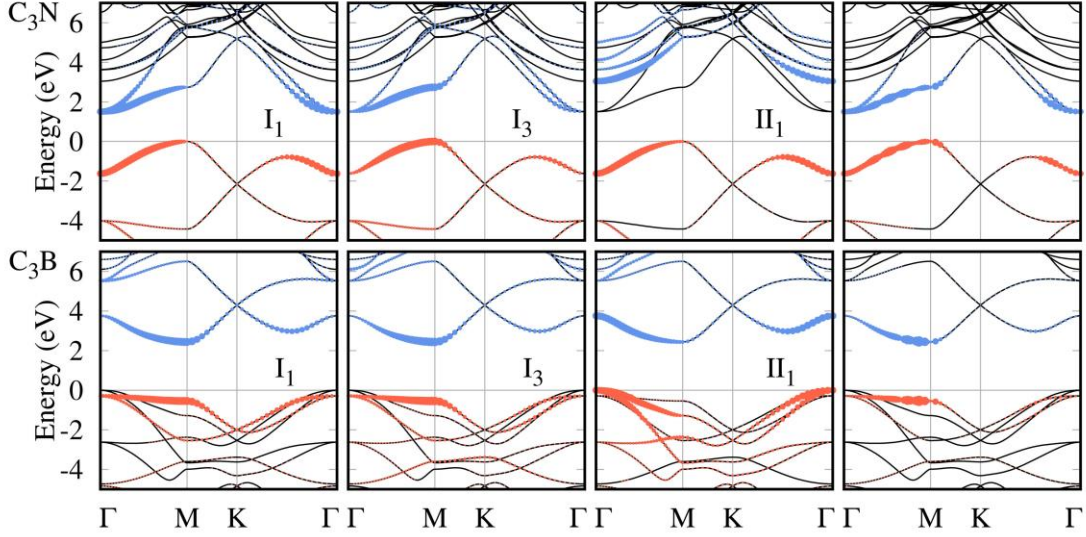


Figure 5. The  $k$ -dependent electron and hole amplitudes  $|A_{ck}^S|^2$  and  $|A_{vk}^S|^2$ . The left three panels are for excitonic states (labeled I<sub>1</sub>, I<sub>3</sub>, and II<sub>1</sub>) with large binding energies, and the right panels are for states with small binding energies. Results for C<sub>3</sub>N (C<sub>3</sub>B) are shown in the top (bottom) panels.

For the states with large binding energies, the  $k$ -dependent electron and hole amplitudes  $|A_{ck}^S|^2$  and  $|A_{vk}^S|^2$  vary smoothly (with respect to the wave vector) within a given band (left three panels in Figure 5), suggesting a coherent superposition of relevant non-interacting  $e$ - $h$  states. For states with smaller binding energies, however, they display rather different (wave vector dependent) behaviors. The top right panel of Figure 5 shows  $|A_{ck}^S|^2$  and  $|A_{vk}^S|^2$  for a state taken from the I series of C<sub>3</sub>N with a smaller exciton binding energy of 0.39 eV; the bottom right panel is for a state taken from the I series of C<sub>3</sub>B with a small exciton binding energy of 0.34 eV. The complex modulation pattern in the reciprocal space (e.g., from  $\Gamma$  to M) is in contrast to the smooth variation observed for larger binding energy states. In general, higher energy (i.e., lower binding energy) excitonic states show more complex reciprocal modulation patterns.

For direct (or quasi-direct) band gap semiconductors, bound excitonic states are often analogized to the Rydberg series of a vastly simplified (3D or 2D) hydrogenic model. These states are often visualized in the reciprocal space space [31] by plotting the  $e$ - $h$  pair amplitudes  $|A^S(\mathbf{k})|^2$  [defined in Eq. (8)]. For indirect gap semiconductors such as C<sub>3</sub>N and C<sub>3</sub>B, such an analogy cannot be easily applied. To better illustrate this point, we show in Figure 6 color contour plots of the

wave vector resolved  $e$ - $h$  pair amplitude  $|A^S(\mathbf{k})|^2$  for the 15 lowest excitonic states of  $\text{C}_3\text{N}$ . These states have exciton binding energies [defined in Eq. (4)] ranging from 1.06 to 0.63 eV within series I as shown in Figure 3.

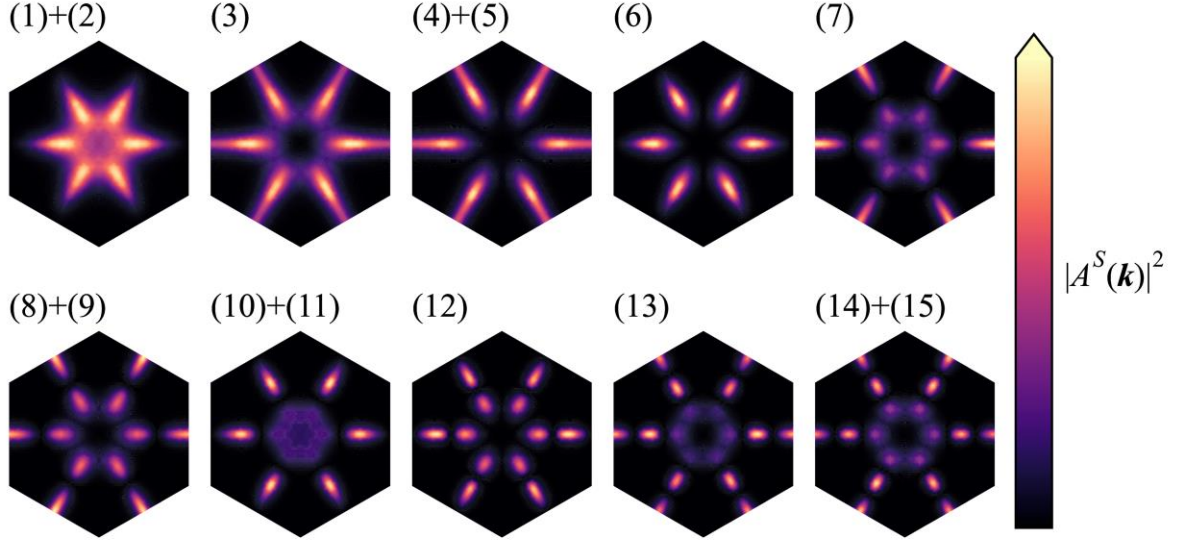


Figure 6. Color contour plots of the  $k$ -resolved  $e$ - $h$  pair amplitudes  $|A^S(\mathbf{k})|^2$  of 15 states with the lowest energy (i.e., highest binding energy) of  $\text{C}_3\text{N}$ . The  $e$ - $h$  pair amplitude develops more complex modulation patterns in the BZ as the excitation energy increases. For degenerate states, we average their amplitudes to show the full symmetry.

With the increasing excitation energy (decreasing binding energy), excitonic states develop more complex mode patterns in the BZ. Therefore, different excitonic states formed primarily within a given pair of valence and conduction bands (with small admixture of other bands) can be viewed as excitation modes in the reciprocal space. The higher the excitation energy, the more complex the mode pattern appears. It then becomes clear that extremely high density  $k$ -grids may be needed to describe excitonic states with very complex mode patterns in the BZ.

Finally, we would like to address another important issue of the formation of excitonic states that has not been carefully investigated so far. Although in principle all valence and conduction states participate in the formation of excitonic states [see Eq. (2)], only free  $e$ - $h$  pairs with close quasiparticle excitation energies will couple strongly, and there has been little understanding on the spread of the free  $e$ - $h$  pairs in the energy domain. To this end, we define, for a given excitonic state  $|S\rangle$ , an  $e$ - $h$  pair participation density of state,

$$PD_{eh}(\omega) = \sum_{v\mathbf{k}} |A_{v\mathbf{k}}^S|^2 \delta(E_{c\mathbf{k}} - E_{v\mathbf{k}} - \omega), \quad (9)$$

which essentially shows the spread in the excitation energies of the non-interacting  $e$ - $h$  pairs that compose the state  $|S\rangle$ . The left panel of Figure 7 shows  $PD_{eh}(\omega)$  for six excitonic states of  $\text{C}_3\text{N}$ ,

three each from the I and II series with the largest exciton binding energies. The full width at half maximum (FWHM) is about 0.3 eV for  $I_1$ ,  $I_2$ , and  $I_3$ , and it is about 0.2 eV for the II series states. Indeed, excitonic states tend to form mostly from the superposition of free  $e$ - $h$  pairs with close (non-interacting) excitation energies. However, the tails can spread to about 1 eV. Interestingly, we find that this 0.2 ~ 0.3 eV FWHM spread is nearly universal, which does not seem to correlate with the exciton binding energy. For example, the middle panels show  $PD_{eh}(\omega)$  for three states each from the I and II series. These states have exciton binding energies of about 0.3 eV. The spreads of  $PD_{eh}(\omega)$  for these small-binding-energy states are qualitatively the same as those of large-binding-energy states. The right panel shows  $PD_{eh}(\omega)$  for three excitonic states that do not belong to the I or II series, which again show similar behaviors as those shown in the left and middle panels. These results suggest that, regardless of the binding energy, excitonic states are formed primarily from free  $e$ - $h$  pairs with similar (non-interacting) pair excitation energies; the spread of the pair excitation energies then reveals the characteristic  $e$ - $h$  interaction strength in these systems.

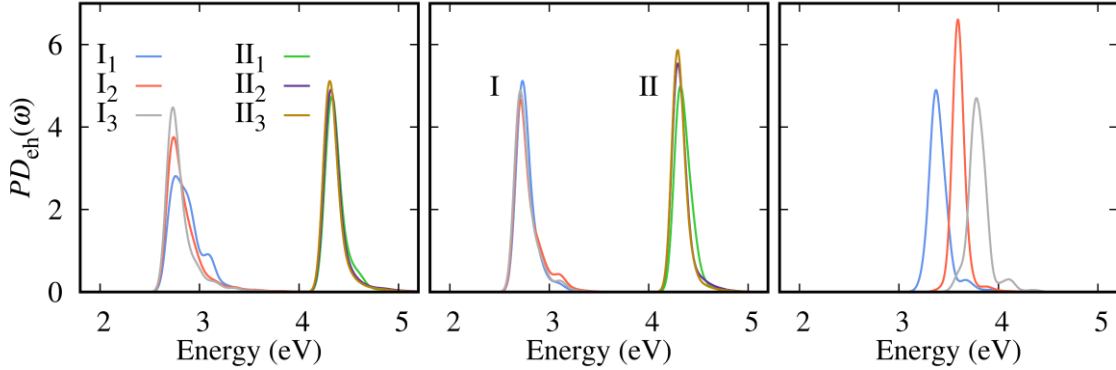


Figure 7. The  $e$ - $h$  pair participation density of selected excitonic state of  $C_3N$ . Left: states with the largest binding energies from the I and II series. Middle: a few states with small binding energies from the I and II series. Right: states with small binding energy between the I and II excitonic series.

#### 4. SUMMARY

In summary, we have investigated the excitonic structures and optical properties of monolayer  $C_3N$  and  $C_3B$  using a GW plus BSE many-body perturbation approach. Both  $C_3N$  and  $C_3B$  have nearly parallel valence and conduction bands spanning an extended region of the BZ, offering a large number of (free)  $e$ - $h$  pair states with nearly identical energies. We find that the coherent superposition of these  $e$ - $h$  pairs results in extremely strong and narrow-band excitonic absorption, making these materials potential candidates for applications in areas such as optical sensing or narrow band optical detectors. In fact, a single pair of degenerate bound excitonic states accounts for over 90% (80%) of the dipole absorption weight below 5 eV for  $C_3N$  ( $C_3B$ ), a remarkable property that has not been observed in any other known 2D materials. Careful examination of the state-specific exciton binding energies unveils a unique shell-like distribution of the exciton states; each shell (series) converges to a distinct excitation edge that can be traced to a set of (nearly)

parallel valence and conduction bands. In addition, large binding energy (around 1 eV or above) exciton states can be found within each series, suggesting that strongly bound excitonic states can form well above the fundamental gap. We further investigate the internal structure and formation mechanism of the excitonic states in C<sub>3</sub>N and C<sub>3</sub>B by analyzing the *e-h* pair amplitude functions in the band, energy and reciprocal space. The band and *k*-resolved electron and hole amplitudes clearly illustrate the band/wave-vector origins of the excitonic states, whereas the pair amplitude function provides a fresh perspective on the excitation modes in the reciprocal space.

### **Acknowledgments**

This work is supported by the National Science Foundation under Grants No. DMR-1506669 and DMREF-1626967. Work at SUSTECH and SHU is supported by the National Natural Science Foundation of China (Grant No. 12104207 and 11929401). We acknowledge computational support from the Center for Computational Research, University at Buffalo, SUNY and the Center for Computational Science and Engineering at Southern University of Science and Technology.

## References

- [1] K. S. Novoselov, A. K. Geim, S. V. Morozov, D. Jiang, Y. Zhang, S. V. Dubonos, I. V. Grigorieva, and A. A. Firsov, Electric Field Effect in Atomically Thin Carbon Films, *Science* **306**, 666 (2004).
- [2] A. Splendiani, L. Sun, Y. Zhang, T. Li, J. Kim, C.-Y. Chim, G. Galli, and F. Wang, Emerging Photoluminescence in Monolayer MoS<sub>2</sub>, *Nano Letters* **10**, 1271 (2010).
- [3] V. Singh, D. Joung, L. Zhai, S. Das, S. I. Khondaker, and S. Seal, Graphene based materials: Past, present and future, *Progress in Materials Science* **56**, 1178 (2011).
- [4] M. Naguib, M. Kurtoglu, V. Presser, J. Lu, J. Niu, M. Heon, L. Hultman, Y. Gogotsi, and M. W. Barsoum, Two-Dimensional Nanocrystals Produced by Exfoliation of Ti<sub>3</sub>AlC<sub>2</sub>, *Advanced Materials* **23**, 4248 (2011).
- [5] R. Mas-Ballesté, C. Gómez-Navarro, J. Gómez-Herrero, and F. Zamora, 2D materials: to graphene and beyond, *Nanoscale* **3**, 20 (2011).
- [6] K. S. Novoselov, A. Mishchenko, A. Carvalho, and A. H. Castro Neto, 2D materials and van der Waals heterostructures, *Science* **353**, aac9439 (2016).
- [7] S. Manzeli, D. Ovchinnikov, D. Pasquier, O. V. Yazyev, and A. Kis, 2D transition metal dichalcogenides, *Nature Reviews Materials* **2**, 17033 (2017).
- [8] M. Gibertini, M. Koperski, A. F. Morpurgo, and K. S. Novoselov, Magnetic 2D materials and heterostructures, *Nature Nanotechnology* **14**, 408 (2019).
- [9] L. S. Panchakarla, K. S. Subrahmanyam, S. K. Saha, A. Govindaraj, H. R. Krishnamurthy, U. V. Waghmare, and C. N. R. Rao, Synthesis, Structure, and Properties of Boron- and Nitrogen-Doped Graphene, *Adv Mater* **21**, 4726 (2009).
- [10] L. Zhao, R. He, K. T. Rim, T. Schiros, K. S. Kim, H. Zhou, C. Gutierrez, S. P. Chockalingam, C. J. Arguello, L. Palova, D. Nordlund, M. S. Hybertsen, D. R. Reichman, T. F. Heinz, P. Kim, A. Pinczuk, G. W. Flynn, and A. N. Pasupathy, Visualizing Individual Nitrogen Dopants in Monolayer Graphene, *Science* **333**, 999 (2011).
- [11] H. Wang, T. Maiyalagan, and X. Wang, Review on Recent Progress in Nitrogen-Doped Graphene: Synthesis, Characterization, and Its Potential Applications, *ACS Catalysis* **2**, 781 (2012).
- [12] Z. Shi, A. Kutana, and B. I. Yakobson, How Much N-Doping Can Graphene Sustain? , *The Journal of Physical Chemistry Letters* **6**, 106 (2015).
- [13] Y. Deng, Y. Xie, K. Zou, and X. Ji, Review on recent advances in nitrogen-doped carbons: preparations and applications in supercapacitors, *Journal of Materials Chemistry A* **4**, 1144 (2016).
- [14] J. Mahmood, E. K. Lee, M. Jung, D. Shin, I.-Y. Jeon, S.-M. Jung, H.-J. Choi, J.-M. Seo, S.-Y. Bae, S.-D. Sohn, N. Park, J. H. Oh, H.-J. Shin, and J.-B. Baek, Nitrogenated holey two-dimensional structures, *Nat Commun* **6**, 6486 (2015).
- [15] H. J. Xiang, B. Huang, Z. Y. Li, S. H. Wei, J. L. Yang, and X. G. Gong, Ordered Semiconducting Nitrogen-Graphene Alloys, *Physical Review X* **2**, 011003 (2012).
- [16] J. Mahmood, E. K. Lee, M. Jung, D. Shin, H.-J. Choi, J.-M. Seo, S.-M. Jung, D. Kim, F. Li, M. S. Lah, N. Park, H.-J. Shin, J. H. Oh, and J.-B. Baek, Two-dimensional polyaniline (C<sub>3</sub>N) from carbonized organic single crystals in solid state, *Proceedings of the National Academy of Sciences* **113**, 7414 (2016).
- [17] S. Yang, W. Li, C. Ye, G. Wang, H. Tian, C. Zhu, P. He, G. Ding, X. Xie, Y. Liu, Y. Lifshitz, S.-T. Lee, Z. Kang, and M. Jiang, C<sub>3</sub>N—A 2D Crystalline, Hole-Free, Tunable-Narrow-Bandgap Semiconductor with Ferromagnetic Properties, *Advanced Materials* **29**, 1605625 (2017).



- [18] Y. Wu, W. Xia, W. Gao, F. Jia, P. Zhang, and W. Ren, Quasiparticle electronic structure of honeycomb C<sub>3</sub>N: from monolayer to bulk, *2d Mater* **6**, 015018 (2019).
- [19] J. Kouvetakis, R. B. Kaner, M. L. Sattler, and N. Bartlett, A novel graphite-like material of composition BC<sub>3</sub>, and nitrogen–carbon graphites, *Journal of the Chemical Society, Chemical Communications*, 1758 (1986).
- [20] H. Tanaka, Y. Kawamata, H. Simizu, T. Fujita, H. Yanagisawa, S. Otani, and C. Oshima, Novel macroscopic BC<sub>3</sub> honeycomb sheet, *Solid State Commun* **136**, 22 (2005).
- [21] X. Luo, J. Yang, H. Liu, X. Wu, Y. Wang, Y. Ma, S.-H. Wei, X. Gong, and H. Xiang, Predicting Two-Dimensional Boron–Carbon Compounds by the Global Optimization Method, *J Am Chem Soc* **133**, 16285 (2011).
- [22] Y. Wu, W. Xia, Y. Zhang, W. Zhu, W. Zhang, and P. Zhang, Remarkable Band-Gap Renormalization via Dimensionality of the Layered Material  $\text{C}_{-3}\text{B}$ , *Physical Review Applied* **14**, 014073 (2020).
- [23] P. Cui, J.-H. Choi, C. Zeng, Z. Li, J. Yang, and Z. Zhang, A Kinetic Pathway toward High-Density Ordered N Doping of Epitaxial Graphene on Cu(111) Using C<sub>5</sub>NCl<sub>5</sub> Precursors, *Journal of the American Chemical Society* **139**, 7196 (2017).
- [24] A. Du, S. Sanvito, and S. C. Smith, First-Principles Prediction of Metal-Free Magnetism and Intrinsic Half-Metallicity in Graphitic Carbon Nitride, *Physical Review Letters* **108**, 197207 (2012).
- [25] A. Thomas, A. Fischer, F. Goettmann, M. Antonietti, J.-O. Müller, R. Schlögl, and J. M. Carlsson, Graphitic carbon nitride materials: variation of structure and morphology and their use as metal-free catalysts, *J Mater Chem* **18**, 4893 (2008).
- [26] W.-J. Ong, L.-L. Tan, Y. H. Ng, S.-T. Yong, and S.-P. Chai, Graphitic Carbon Nitride (g-C<sub>3</sub>N<sub>4</sub>)-Based Photocatalysts for Artificial Photosynthesis and Environmental Remediation: Are We a Step Closer To Achieving Sustainability? , *Chem Rev* **116**, 7159 (2016).
- [27] B. Mortazavi, M. Shahrokhi, M. Raeisi, X. Zhuang, L. F. C. Pereira, and T. Rabczuk, Outstanding strength, optical characteristics and thermal conductivity of graphene-like BC<sub>3</sub> and BC<sub>6</sub>N semiconductors, *Carbon* **149**, 733 (2019).
- [28] A. Bafekry, Graphene-like BC<sub>6</sub>N single-layer: Tunable electronic and magnetic properties via thickness, gating, topological defects, and adatom/molecule, *Physica E: Low-dimensional Systems and Nanostructures* **118**, 113850 (2020).
- [29] A. Bafekry and C. Stampfl, Band-gap control of graphenelike borocarbonitride  $\text{g}\text{-}\text{BC}_{-6}\text{N}$  bilayers by electrical gating, *Phys Rev B* **102**, 195411 (2020).
- [30] B. Mortazavi, Ultrahigh thermal conductivity and strength in direct-gap semiconducting graphene-like BC<sub>6</sub>N: A first-principles and classical investigation, *Carbon* **182**, 373 (2021).
- [31] D. Y. Qiu, F. H. da Jornada, and S. G. Louie, Screening and many-body effects in two-dimensional crystals: Monolayer  $\text{MoS}_{-2}$ , *Physical Review B* **93**, 235435 (2016).
- [32] D. Y. Qiu, F. H. da Jornada, and S. G. Louie, Environmental screening effects in 2D materials: renormalization of the bandgap, electronic structure, and optical spectra of few-layer black phosphorus, *Nano letters* **17**, 4706 (2017).
- [33] M. S. Hybertsen and S. G. Louie, Electron correlation in semiconductors and insulators: Band gaps and quasiparticle energies, *Phys Rev B* **34**, 5390 (1986).
- [34] M. Rohlfing and S. G. Louie, Electron-hole excitations and optical spectra from first principles, *Physical Review B* **62**, 4927 (2000).

- [35] J. Deslippe, G. Samsonidze, D. A. Strubbe, M. Jain, M. L. Cohen, and S. G. Louie, BerkeleyGW: A massively parallel computer package for the calculation of the quasiparticle and optical properties of materials and nanostructures, *Comput Phys Commun* **183**, 1269 (2012).
- [36] W. Kohn and L. J. Sham, Self-Consistent Equations Including Exchange and Correlation Effects, *Physical Review* **140**, A1133 (1965).
- [37] D. M. Ceperley and B. J. Alder, Ground State of the Electron Gas by a Stochastic Method, *Phys Rev Lett* **45**, 566 (1980).
- [38] J. P. Perdew and A. Zunger, Self-interaction correction to density-functional approximations for many-electron systems, *Phys Rev B* **23**, 5048 (1981).
- [39] W. Gao, W. Xia, X. Gao, and P. Zhang, Speeding up GW Calculations to Meet the Challenge of Large Scale Quasiparticle Predictions, *Scientific Reports* **6**, 36849 (2016).
- [40] W. Xia, W. Gao, G. Lopez-Candales, Y. Wu, W. Ren, W. Zhang, and P. Zhang, Combined subsampling and analytical integration for efficient large-scale GW calculations for 2D systems, *npj Computational Materials* **6**, 118 (2020).
- [41] S. Ismail-Beigi, Truncation of periodic image interactions for confined systems, *Physical Review B* **73**, 233103 (2006).
- [42] J. Klimeš, D. R. Bowler, and A. Michaelides, Van der Waals density functionals applied to solids, *Physical Review B* **83**, 195131 (2011).